arXiv:2609.15775v1 [cond-mat.mtrl-sci] 14 Sep 2026

Proximity-induced charge density waves in a moiré heterobilayer

Christopher T. S. Cheung,[1] Arash A. Mostofi,[2] and Johannes Lischner[2]

[1]*Departments of Physics and Materials and the Thomas Young Centre for Theory and Simulation of Materials, Imperial College London, South Kensington Campus, London SW7 2AZ, UK*

[2]*Departments of Physics and Materials and the Thomas Young center for Theory and Simulation of Materials, Imperial College London, South Kensington Campus, London SW7 2AZ, UK*

(Dated: September 15, 2026)

Twisted heterobilayers of two-dimensional materials have emerged as a platform for studying emergent phases of matter. In this work, we investigate charge density waves (CDW) in a twisted $NbSe_2/MoSe_2$ bilayer using first-principles calculations. We observe CDW formation in both layers, even though $MoSe_2$ does not feature a CDW in its monolayer form. Moreover, we find that the CDW is highly non-uniform with filled-center, hollow-center and hexagonal CDWs coexisting in the moiré unit cells of both layers. We assess different mechanisms of CDW formation in the $MoSe_2$ layer and conclude that the dominant one is the steric repulsion between Se atoms across the van der Waals gap. The strength of this effect is highly sensitive to the interlayer separation, which explains why the CDW amplitude in the $MoSe_2$ layer depends strongly on the local stacking arrangement. Our work demonstrates that novel broken-symmetry phases can be induced in twisted heterobilayers through proximity effects.

INTRODUCTION

Twisted moiré bilayers are tunable platforms for studying novel electronic, optical and structural properties [1–16]. For example, twisted bilayers of WSe_2 and $MoSe_2$ host moiré-trapped interlayer excitons [17] and localization of intralayer excitons in twisted WS_2/WSe_2 bilayers enables realization of the Bose-Hubbard model [18]. While twisted bilayers formed by semiconducting monolayers have been studied extensively, bilayers involving metallic monolayers have received less attention.

Metallic 2D materials often exhibit symmetry-broken ground states. For example, the metallic transition metal dichalcogenide (TMD) monolayer $NbSe_2$ hosts a charge density wave (CDW) and superconductivity at low temperatures [19, 20]. CDWs in $NbSe_2$ are formed when the Nb atoms displace from their high-symmetry positions to break the translational and threefold rotational symmetries. Different CDW types have been observed in $NbSe_2$ including filled-center CDWs (where Nb atoms move towards Se atoms), hollow-center CDWs (Nb atoms move towards interstitial sites) and hexagonal CDWs (Nb atoms move towards other Nb atoms) [21–23]. As these different CDWs have very similar energies, their relative stability can be controlled by doping and strain [24]. When two $NbSe_2$ monolayers are combined into a twisted homobilayer, the CDWs in each monolayer become highly non-uniform as a consequence of the inhomogeneous strain induced by moiré relaxations and different CDW types, including one-dimensional stripe CDWs, coexist in the moiré unit cell [25].

Apart from metallic 2D materials which often feature intrinsic CDWs, it is also possible to induce CDWs in semiconducting monolayers by charge doping or interfacing with other monolayers [20, 26]. For example, it was demonstrated that CDWs can be induced in the semiconducting monolayer MoS_2 by electron doping [27]. Also, it is possible to induce a CDW in semi-metallic graphene by interfacing it with $NbSe_2$ [28]. However, the possibility of inducing CDWs in twisted heterobilayers through a proximity effect has not been studied so far.

In this work, we carry out first-principles relaxation of twisted moiré bilayers of $NbSe_2/MoSe_2$ using density functional theory and use a novel approach for revealing the presence, type and amplitude of inhomogeneous CDWs in the moiré unit cell. We find that weak non-uniform CDWs are induced in the $MoSe_2$ layer due to the interaction with the $NbSe_2$. By studying CDWs in untwisted bilayers, we demonstrate that the mechanism underpinning CDW formation in $MoSe_2$ is the steric repulsion between Se atoms across the van der Waals gap between the two layers. Our work demonstrate that structural symmetry broken phases can be induced in semiconducting monolayers by forming twisted moiré bilayers, and potentially offer a route to induce superconducting states in these systems.

METHODOLOGY

We construct a $NbSe_2/MoSe_2$ bilayer with a twist angle of 3.15° (containing 1,986 atoms in the moiré unit cell) using the procedure described in Ref. [29]. The unit cell lattice constant is taken to be that of an untwisted antiparallel $NbSe_2/MoSe_2$ bilayer ($a_0 = 3.42$ Å) obtained by performing a first-principles DFT relaxation using the optB88-vdw exchange-correlation functional as implemented in the SIESTA code [30, 31]. This is the lattice constant of the MM stacked untwisted bilayer, which is the most stable stacking. Note that the lattice constants of the AB and XX stacked untwisted bilayers are very similar (both are 3.41 Å) to the MM value. We

then perform a first-principles atomic relaxation of the twisted bilayer. The construction of the moiré unit cell and the additional computational details are provided in Section S1 of the Supplementary Materials.

We analyze the formation of charge density waves (CDWs) in the twisted bilayer using the smeared metal atomic (either Mo or Nb) density. The smeared atomic density at a position $\mathbf{r}$ is computed by placing gaussian functions on every Mo and Nb atom, and summing over all the gaussian functions within a cutoff radius within a given layer of the bilayer around that point (for computational efficiency) [25]. Mathematically,

$$\rho(\mathbf{r}) = \frac{1}{2\pi\sigma^2}\sum_{i=1}^{N}\exp\left(-\frac{(\mathbf{r}-\mathbf{R}_i)^2}{2\sigma^2}\right), \tag{1}$$

where N is the number of metal atoms in the given layer within the cutoff radius, $\mathbf{R}_i$ is the relaxed position of the i-th metal atom and σ is a smearing parameter. By using a smearing parameter that is comparable to the unit cell lattice constant a_0, local changes in the Nb–Nb distances give rise to a modulation in the smeared atomic density. This allows us to reveal any CDW formation.

In high-symmetry monolayer $NbSe_2$, there are three soft phonon modes with wavevectors $\mathbf{q}_1 = \frac{2\pi}{3\sqrt{3}a_0}(1,-\sqrt{3})$, $\mathbf{q}_2 = \frac{2\pi}{3\sqrt{3}a_0}(1,\sqrt{3})$ and $\mathbf{q}_3 = \frac{2\pi}{3\sqrt{3}a_0}(-2,0)$. These soft modes give rise to CDW formation in the monolayer. The corresponding atomic displacements are given by

$$\delta\mathbf{R}_i = \sum_{j=1}^{3} v_j\hat{\mathbf{q}}_j\cos(\mathbf{q}_j\cdot\mathbf{R}_i+\varphi_j), \tag{2}$$

where v_j and φ_j are the displacement amplitudes and the phases of displacement along the CDW wavevectors, respectively [32]. The Nb displacements of the hollow-center, filled-center, and hexagonal CDWs are shown in Figure 1(a), (b), and (c) respectively. Each CDW type is characterized by a specific combination of phases φ_j which are summarized in Table S1 of the Supplementary Materials.

Similar to the relaxed atomic positions, the smeared Nb atom density of the $NbSe_2$ monolayer in the CDW state can also be approximated as a Fourier series according to

$$\tilde{\rho}(\mathbf{r}) = \tilde{\rho}_0 + \sum_{j=1}^{3}\tilde{\rho}_j\cos(\mathbf{q}_j\cdot\mathbf{r}+\phi_j), \tag{3}$$

where $\tilde{\rho}_0$ is the mean atomic density, $\tilde{\rho}_j$ is the density oscillation amplitude along $\mathbf{q}_j$, and ϕ_j is the phase of the oscillation along $\mathbf{q}_j$.

For uniform CDWs, the amplitudes of the density oscillation ($\tilde{\rho}_j$) are proportional to the magnitude of the atomic displacements (v_j), while the phases of the density oscillation (ϕ_j) characterize the displacement patterns. This is because the values of ϕ_j determine the positions of the maxima in the smeared atomic density relative to some chosen origin. For the filled-center, hollow-center, and hexagonal CDWs, the density maxima are located at Se, hollow, and Nb sites, respectively. Each CDW is therefore associated with a distinct combination of phases. Conversely, one can use the phases to identify the CDW type.

The smeared Nb atom density of the hollow-center CDW, computed using $\sigma = 0.85a_0$, is shown in Figure 1(d). The observed modulation of the smeared atomic density can be viewed as a standing wave obtained by superposing the three density oscillations along each wavevector. The smeared Nb atom densities of the filled-center and hexagonal CDWs are shown in Figures 1(e) and (f), respectively. Similar interference patterns are observed, but the density maxima and minima have different positions compared to that of the hollow-center CDW.

In twisted bilayers, different types of CDWs can coexist in the moiré unit cell [25]. This is because the different CDW types have very similar energies and small changes in the local strain can give rise to a different energetic ordering. In our calculations, the hollow-center CDW is most stable but the total energies (per 3×3 unit cell) of the filled-center and hexagonal CDWs are only about 20-30 meV higher, see Table S2 of Supplementary Materials. To describe such a twisted bilayer system, we allow the mean density, the amplitudes and phases of the smeared atomic density to vary over space according to

$$\tilde{\rho}(\mathbf{r}) = \tilde{\rho}_0(\mathbf{r}) + \sum_{j=1}^{3}\tilde{\rho}_j(\mathbf{r})\cos(\mathbf{q}_j\cdot\mathbf{r}+\phi_j(\mathbf{r})). \tag{4}$$

To determine the $\tilde{\rho}_j(\mathbf{r})$ and $\phi_j(\mathbf{r})$ from a given smeared atomic density corresponding to a relaxed atomic structure, we proceed as follows: first, the three phase fields $\phi_j(\mathbf{r})$ are obtained by repeatedly projecting gradients of the smeared metal atom density onto unit vectors $\hat{\mathbf{n}}_j$ that are orthogonal to the corresponding CDW wavevector $\mathbf{q}_j$ (see Section S3 of the Supplementary Materials for the derivation). For example, $\phi_1(\mathbf{r})$ is extracted from

$$\tan(\mathbf{q}_1\cdot\mathbf{r}+\phi_1(\mathbf{r})) = -\frac{1}{|\mathbf{q}_1|^2}\frac{\mathbf{q}_1\cdot\nabla(\hat{\mathbf{n}}_2\cdot\nabla(\hat{\mathbf{n}}_3\cdot\nabla\rho(\mathbf{r})))}{\hat{\mathbf{n}}_2\cdot\nabla(\hat{\mathbf{n}}_3\cdot\nabla\rho(\mathbf{r}))}. \tag{5}$$

From the values of these phases, the local CDW type can be identified, see Section S3 of the Supplementary Materials for additional details.

Next, the mean density $\tilde{\rho}_0(\mathbf{r})$ and the density oscillation amplitudes $\tilde{\rho}_j(\mathbf{r})$ are determined numerically by minimizing the Lagrangian

$$\mathcal{L} = \int(\tilde{\rho}(\mathbf{r})-\rho(\mathbf{r}))^2 d^2\mathbf{r}. \tag{6}$$

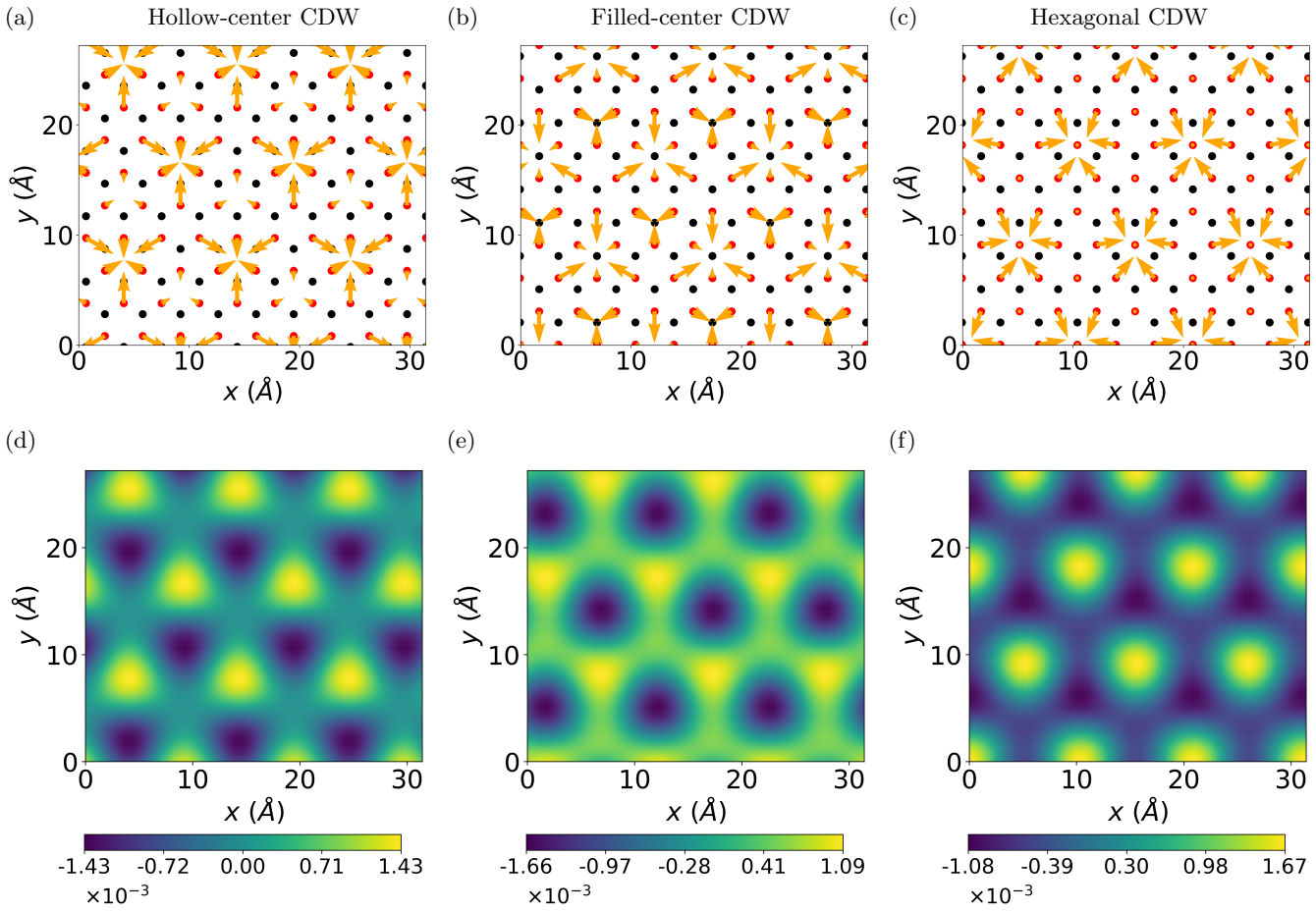


FIG. 1: Top panels: atomic displacements (orange arrows) of Nb atoms (red circles) in different CDW states. Bottom panels: corresponding smeared Nb density in units of Å^{-2}. Black circles indicate Se atoms. For clarity, we show the difference between the smeared Nb density and its mean value.

Note that $\tilde{\rho}(\mathbf{r})$ denotes the approximated atomic density defined in Equation 4 and $\rho(\mathbf{r})$ denotes the exact smeared atomic density defined in Equation 1. By minimizing this Lagrangian, the parameters $\{\tilde{\rho}_j\}$ that give the best fit to the the actual smeared atomic density are determined. Specifically, the four Euler-Lagrange equations representing the variation of $\mathcal{L}$ with respect to $\tilde{\rho}_0(\mathbf{r})$ and $\tilde{\rho}_j(\mathbf{r})$ are derived and solved using the steepest descent method. This allows us to deduce the "CDW field" in the given layer. More details of the implementation is included in Section S5 in the Supplementary Materials.

RESULTS

Figure 2(a) shows the smeared Nb density $\rho(\mathbf{r})$ for $\sigma = 0.85a_0$ for the twisted $NbSe_2/MoSe_2$ bilayer. The smeared Nb density exhibits a modulation characteristic of the formation of a CDW. In contrast to the smeared Nb density of the monolayer shown in Fig. 1, the smeared Nb density of the twisted bilayer does not exhibit a regular modulation pattern throughout the moiré unit cell, indicating the co-existence of different CDW types. [33]

To identify which CDW types co-exist in the $NbSe_2$ layer of the twisted bilayer, we calculate the phase fields $\phi_j(\mathbf{r})$ and compare their values to those of the uniform CDW phases of the monolayer. Fig. 2(c) shows that filled-center, hollow-center and hexagonal CDWs are all observed. In particular, a large area of hollow-center CDW is found around the MM center of the unit cell. This region is surrounded by smaller patches of filled-center CDWs and hexagonal CDWs.

We now turn our attention to the $MoSe_2$ layer of the $NbSe_2/MoSe_2$ twisted bilayer. Figure 2(b) shows the smeared Mo density for $\sigma = 0.85a_0$. Even though monolayer $MoSe_2$ does not exhibit a CDW, the smeared Mo density exhibits a modulation characteristic of CDW formation. However, the amplitude of the CDW modulations is approximately an order of magnitude smaller than in the $NbSe_2$ layer. Comparing the smeared Mo

density to the smeared Nb density reveals that maxima in the Mo density are aligned with top of minima of the Nb density and vice versa. For example, the Nb density exhibits a maximum at the MM center, while the Mo density exhibits a minimum, see also Figure S2 of the Supplementary Materials.

Again, different types of CDWs can be identified in the $MoSe_2$ layer, as shown in Figure 2(d). Similarly to the $NbSe_2$ layer, a large region of hollow-center CDW is observed in the vicinity of the MM center which is surrounded by smaller regions of filled-center and hexagonal CDWs.

Next, we analyze the CDW displacement amplitudes in more detail, see Fig. 3. In the $NbSe_2$ layer, the CDW displacement amplitudes at the MM, AB, and XX centers are 6.5×10^{-2} Å, 7.7×10^{-2} Å, and 4.8×10^{-2} Å, respectively. In contrast, the CDW displacement amplitudes are about an order of magnitude smaller in the $MoSe_2$ layer: 1.8×10^{-3} Å in the MM stacking region; 1.1×10^{-3} Å in the AB region; and 0.7×10^{-3} Å in the XX region.

These observations raise the question, "what is the microscopic mechanism that drives the formation of CDWs in the $MoSe_2$ layer?". To answer this, we study CDW formation in untwisted $NbSe_2/MoSe_2$ bilayers with AB, XX, and MM stacking. Specifically, we first relax the three untwisted bilayers using a 3×3 supercell. We then inspect the atomic displacement vectors in both layers of an MM stacked untwisted bilayer, see Fig. 4. We focus on the displacement vectors of the inner Se atoms of each layer and of the Mo atoms. It can be observed that the inner Se atoms of the $MoSe_2$ layer (grey circles) tend to move in the opposite direction to the Se atoms of the $NbSe_2$ layer (black circles), while the Mo atoms (orange circles) move in the same direction as the Se atoms they are bonded to. The same behavior is found for the XX and AB bilayers, see Figures S3 of the Supplementary Materials. This suggests that the formation of CDWs in the $MoSe_2$ layer is mediated by the steric repulsion between the inner Se atoms of the two layers: the CDW formation in the $NbSe_2$ layer induces a displacement of the Se atoms; to reduce steric repulsion, the inner Se atoms of the $MoSe_2$ layer move "out of the way"; this, in turn, drives the displacements of the Mo atoms to reduce the distortion of the Mo–Se bonds. As a consequence, Mo atoms avoid positions directly adjacent across the vdW gap between the layers Nb atoms explaining why maxima of the Mo smeared atomic density coincide with minima of the Nb smeared atomic density.

Next, to further establish the correlation between the CDW amplitude in the $MoSe_2$ layer and in the $NbSe_2$ layer, we perform calculations of untwisted bilayers in which we fix the hollow-center CDW amplitude in the $NbSe_2$ layer. Figure 5 shows that for all bilayers the amplitude of the induced CDW in the $MoSe_2$ increases approximately linearly with the fixed CDW amplitude in the $NbSe_2$ layer.

The above analyses suggest that the dominant mechanism for inducing CDWs in the $MoSe_2$ is steric repulsion. If this is the case, it is expected that the CDW displacements correlates with stacking due to different stackings having different interlayer spacings. Therefore, we calculate the amplitudes of the CDW displacements in the $MoSe_2$ layer, see Table I. We find that CDW displacements in the untwisted bilayers have the same order of magnitude as in the twisted bilayer, but are somewhat smaller for the MM and AB stackings and larger for the XX stacking. This is consistent with the values predicted in Fig. 5. This shows that steric repulsion is the dominant mechanism responsible for CDW formation in the $MoSe_2$ layer.

	$\bar{v}$ (10^{-3} Å)		Interlayer separation (Å)	
	Twisted bilayer	Untwisted bilayer	Twisted bilayer	Untwisted bilayer
MM	1.75	1.08	6.26	6.26
AB	1.13	0.74	6.38	6.37
XX	0.72	0.88	6.75	6.79

TABLE I: Average CDW displacement amplitude $\bar{v}$ of the Mo atoms and interlayer separation in relaxed twisted (3.15°) and untwisted bilayers of $NbSe_2/MoSe_2$.

Having established the microscopic mechanism of CDW formation in the $MoSe_2$ layer, we can now explain the dependence of the CDW amplitude on the bilayer stacking. Steric repulsion is stronger for stackings with small interlayer separation. Indeed, Table I shows that the MM and AB stacking region have smaller interlayer distances compared to the XX stacking region and the largest CDW amplitude is found there. The linear dependence of the $MoSe_2$ CDW amplitude on the $NbSe_2$ CDW amplitude also explains the quantitative differences between untwisted and the twisted bilayers, see Table I: specifically, we extract the $NbSe_2$ CDW amplitude in the various stacking regions from the relaxed atomic structure of the twisted bilayer and use Figure 5 to predict $MoSe_2$ CDW amplitudes. The predicted values are 1.1×10^{-3} Å for the MM region, 1.0×10^{-3} Å for the AB region and 0.6×10^{-3} Å for the XX region. These values are in good agreement to those extracted from the relaxed atomic structure, see Table I. We note that the differences in $NbSe_2$ originate from the local strain induced in the moiré superlattice.

Finally, we note that it has been reported in the literature that charge doping of semiconducting TMD monolayer MoS_2 induces the formation of a CDW [27]. Therefore, we should consider the possibility that the mechanism for the proximity effect that we observe in the $NbSe_2/MoSe_2$ bilayer is a result of charge transfer between the two layers. For this, we analyze the distribution of charge in untwisted bilayers with a fixed CDW in

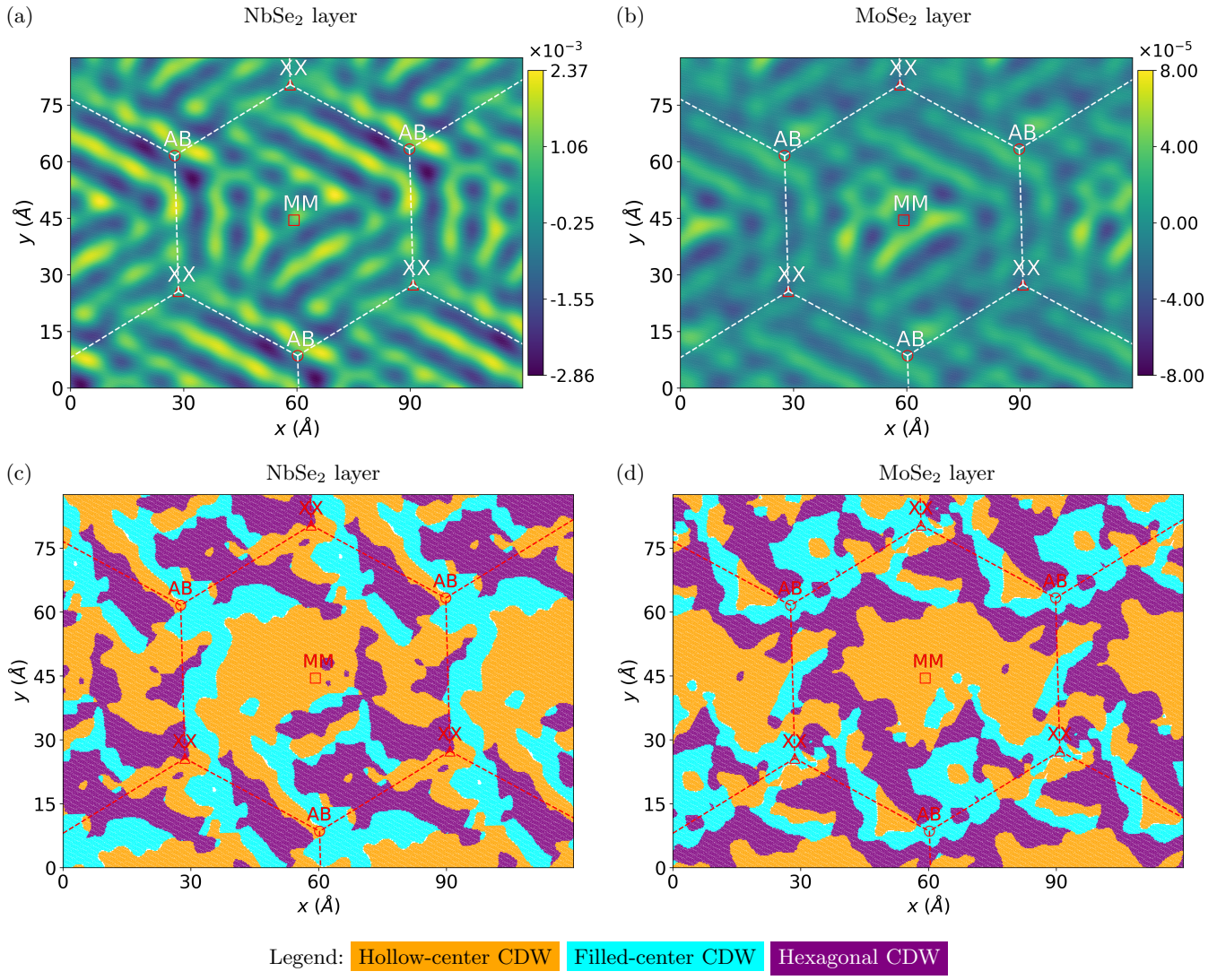


FIG. 2: Smeared atomic densities (in units of Å^{-2}) of Nb atoms (a) and Mo atoms (b) in a 3.15° twisted $MoSe_2/NbSe_2$ bilayer. For clarity, the difference between the smeared atomic density and its mean value is shown. Centers of high-symmetry stacking regions are marked in red, and the Wigner-Seitz cell of the moiré superlattice is indicated in white. Maps of different CDW types in the $NbSe_2$ layer (a) and the $MoSe_2$ layer (b).

the $NbSe_2$ layer. We find that interlayer charge transfer occurs, but the amount of transferred charge does not depend on the CDW amplitude in the $NbSe_2$ layer, as shown in Figure S7 of Supplementary Materials. In the $MoSe_2$ layer, the CDW induced as a result of doping should increase in amplitude as a function of the amount of charge transfer. This then demonstrates that the hypothesis that the proximity effect is due to charge transfer is incompatible with our observation that the charge transfer is constant and independent of CDW amplitude. This suggests that interlayer charge transfer is not the dominant mechanism for CDW formation in the $MoSe_2$ layer.

CONCLUSIONS

In this work, we demonstrated that charge density waves are induced in the semiconducting $MoSe_2$ layer through a proximity effect in a twisted $NbSe_2/MoSe_2$ bilayer. We reveal steric repulsion between Se atoms across the van der Waals gap as the microscopic mechanism driving CDW formation in the $MoSe_2$ layer. As this coupling is highly sensitive to the interlayer distance, the amplitude of the induced CDW depends on the local stacking arrangement. We note that this effect could potentially be used to control superconductivity in the $MoSe_2$ layer [27]. Our work shows that it is possible to engineer symmetry-broken states in 2D materials by con-

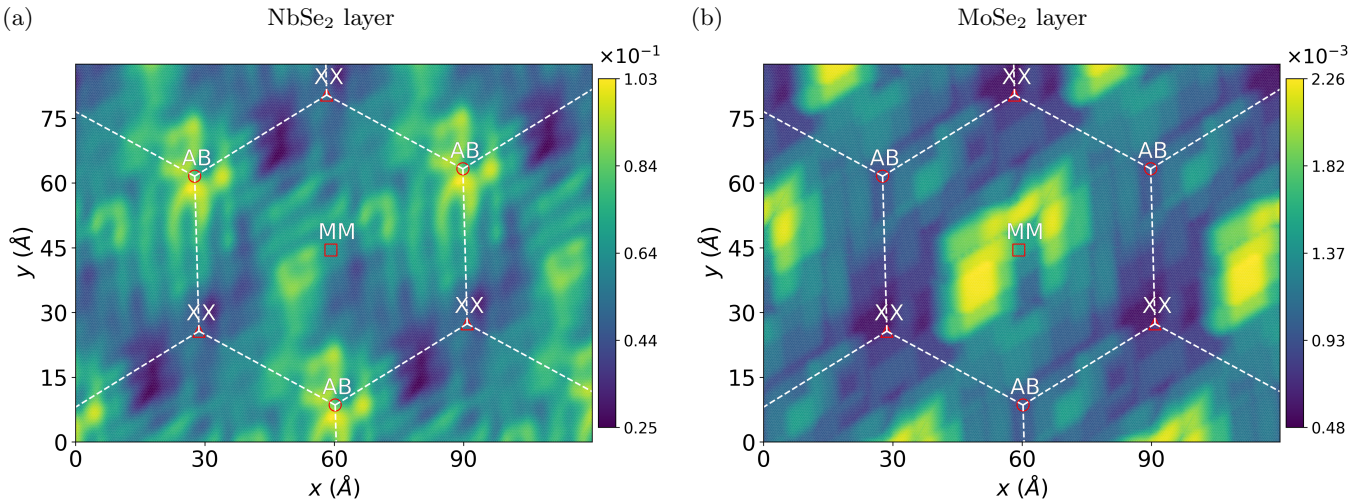


FIG. 3: The average CDW displacement amplitude (in Å) of (a) Nb atoms and (b) Mo atoms in a twisted $MoSe_2/NbSe_2$ bilayer. Centers of high-symmetry stacking regions are marked in red, and the Wigner-Seitz cell of the moiré superlattice is indicated in white.

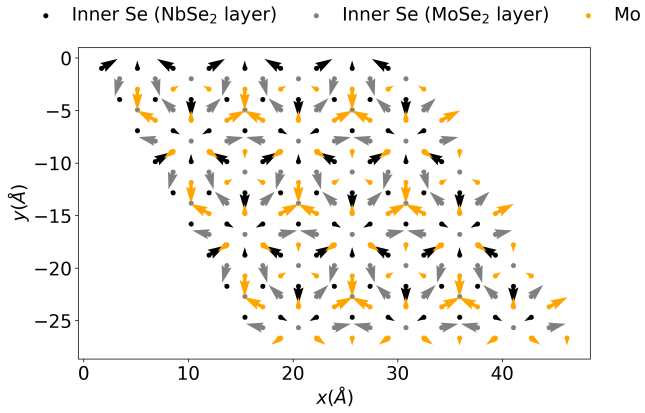


FIG. 4: Atomic displacements of the inner Se atoms in the $NbSe_2$ layer (black), $MoSe_2$ layer (grey), and Mo atoms (orange) in an untwisted MM-stacked bilayer of $NbSe_2/MoSe_2$. The displacements of the inner Se atoms in the $NbSe_2$ layer are multiplied by a factor of 50, while the displacements of the inner Se and Mo atoms in the $MoSe_2$ are multiplied by a factor of 750.

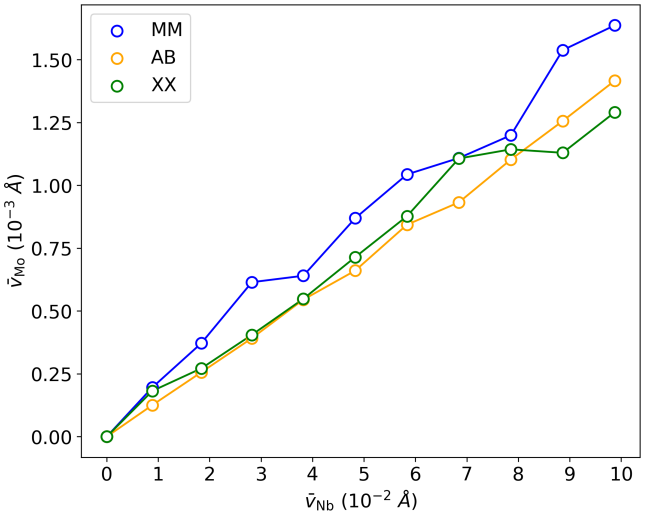


FIG. 5: CDW displacement amplitude in the $MoSe_2$ layer as function of the CDW displacement amplitude in the $NbSe_2$ layer for different untwisted bilayers. In these calculations, a hollow-centered CDW is imposed on the Nb atoms and all other atoms are allowed to relax.

structing twisted heterobilayers.

SUPPLEMENTARY MATERIALS

S1. METHODS

S1.1. Construction of the moiré unit cell

To construct the initial positions for the atomic relaxations, we stack and twist two flat anti-parallel $NbSe_2$ and $MoSe_2$ monolayers that do not feature a charge density wave. The resulting moiré unit cell is spanned by the lattice vectors $\mathbf{t}_1$ and $\mathbf{t}_2$ given by

$$\begin{aligned} \mathbf{t}_1 &= n\mathbf{a}_1 + m\mathbf{a}_2, \\ \mathbf{t}_2 &= -m\mathbf{a}_1 + (n+m)\mathbf{a}_2, \end{aligned} \tag{S1}$$

where $\mathbf{a}_1 = a_0/2(\sqrt{3}, 1, 0)$ and $\mathbf{a}_2 = a_0/2(\sqrt{3}, -1, 0)$, and a_0 is the lattice constant.

The integers n, m are the number of unit cells along each moiré lattice vector. The twist angle is given by $\cos\theta = (n^2 + 4nm + m^2)/[2(n^2 + nm + m^2)]$ [29]. Thus, choosing the pair of integers (n, m) as $(10, 11)$ gives the twist angle of 3.15°. The number of atoms in the moiré unit cell is $N = 6(n^2 + nm + m^2)$, which is 1,986 at the chosen twist angle.

S1.2. Computational details

The large-scale ab initio density functional theory code SIESTA [30] is used for relaxation and electronic structure calculations. To capture van der Waals interactions, the exchange-correlation functional optB88-vdw is used [31]. We use Troullier-Martins pseudopotentials [34], and a double-ζ polarized basis where the "split norm" is 0.583 and the energy shift is 0.0109 Ry. We use Γ-point sampling of the first Brillouin zone. In the self-consistent cycle, the Hamiltonian and the density matrix are converged to 1 μeV and 1×10^{-7} per atom, respectively. The force tolerance is set to 3×10^{-2} eV/Å. The electronic temperature is set to 15.7 K, which is equal to 0.1 mRy. The mesh grid cutoff is 500 Ry.

In the relaxation of the unit cells of the untwisted bilayers of $NbSe_2/MoSe_2$, a Monkh orst-Pack grid of $32 \times 23 \times 1$ is used for the k-point sampling. For the 3×3 cell relaxations, a Monkorst-Pack grid of $10 \times 10 \times 1$ is used. All other parameters are the same as the twisted bilayer relaxation. For the simulation cell, the unit vectors $\mathbf{a}_1' = 3a_0(1, 0, 0)$ and $\mathbf{a}_2' = 3a_0/2(1, -\sqrt{3}, 0)$ are used.

S1.3. Smeared atomic density and its Fourier representation

We now show that the smeared atomic density defined in Equation 1 becomes a Fourier series generated by the three charge density wavevectors when the smearing is comparable to the lattice constant.

Suppose $\mathbf{R}_i$ represents the initial position of the i-th atom in the high-symmetry lattice before any displacement, and is displaced according to the displacement field $\mathbf{R}_i \to \mathbf{R}_i + \delta\mathbf{R}_i$, where $|\delta\mathbf{R}_i| << |\mathbf{R}_i - \mathbf{R}_j|$ for any $i \neq j$, and

$|\delta\mathbf{R}_i| << \sigma$, then the smeared atomic density transforms as,

$$\rho(\mathbf{r}) \to \rho'(\mathbf{r}) \tag{S2}$$

$$= \sum_{i=1}^{N} \exp\left(-\frac{1}{2\sigma^2}(\mathbf{r} - (\mathbf{R}_i + \delta\mathbf{R}_i))^2\right) \tag{S3}$$

$$= \sum_{i=1}^{N} \exp\left(-\frac{1}{2\sigma^2}(\mathbf{r} - \mathbf{R}_i)^2\right) \exp\left(-\frac{1}{\sigma^2}(\mathbf{r} - \mathbf{R}_i)\cdot\delta\mathbf{R}_i\right) \exp\left(-\frac{1}{2\sigma^2}\delta\mathbf{R}_i^2\right) \tag{S4}$$

$$\approx \sum_{i=1}^{N} \exp\left(-\frac{1}{2\sigma^2}(\mathbf{r} - \mathbf{R}_i)^2\right) \exp\left(-\frac{1}{\sigma^2}(\mathbf{r} - \mathbf{R}_i)\cdot\delta\mathbf{R}_i\right) \tag{S5}$$

$$\approx \sum_{i=1}^{N} \exp\left(-\frac{1}{2\sigma^2}(\mathbf{r} - \mathbf{R}_i)^2\right) \left[1 + \left(-\frac{1}{\sigma^2}(\mathbf{r} - \mathbf{R}_i)\cdot\delta\mathbf{R}_i\right)\right] \tag{S6}$$

$$= \rho(\mathbf{r}) - \left(\frac{1}{\sigma^2}\sum_{i=1}^{N} \exp\left(-\frac{1}{2\sigma^2}(\mathbf{r} - \mathbf{R}_i)^2\right)(\mathbf{r} - \mathbf{R}_i)\cdot\delta\mathbf{R}_i\right) \tag{S7}$$

$$\tag{S8}$$

We note that since $\mathbf{R}_i$ represents a high-symmetry lattice, when a smearing comparable to the lattice constant is used, the associated smeared atomic density is simply the average atomic density, ρ_0, which is a constant over space. Also, the normalization factor $1/(2\pi\sigma^2)$ is omitted in the above expressions.

Under a charge density wave, the atomic displacements are given by

$$\delta\mathbf{R}_i = \sum_{j=1}^{3} v^{(j)}\hat{\mathbf{q}}_j \cos(\mathbf{q}_j\cdot\mathbf{R}_i + \varphi_j), \tag{S9}$$

then Equation S8 becomes

$$\rho'(\mathbf{r}) = \rho_0 - \frac{1}{\sigma^2}\sum_{i=1}^{N} \exp\left(-\frac{1}{2\sigma^2}(\mathbf{r} - \mathbf{R}_i)^2\right)(\mathbf{r} - \mathbf{R}_i)\cdot\sum_{j=1}^{3}\hat{\mathbf{q}}_j v^{(j)}\cos(\mathbf{q}_j\cdot\mathbf{R}_i + \varphi_j) \tag{S10}$$

$$= \rho_0 - \frac{1}{\sigma^2}\sum_{i=1}^{N} \exp\left(-\frac{1}{2\sigma^2}(\mathbf{R}'_i)^2\right)\mathbf{R}'_i\cdot\sum_{j=1}^{3}\hat{\mathbf{q}}_j v^{(j)}\cos(\mathbf{q}_j\cdot(\mathbf{r} - \mathbf{R}'_i) + \varphi_j), \tag{S11}$$

$$\tag{S12}$$

by making the change of variable $\mathbf{R}'_i = \mathbf{r} - \mathbf{R}_i$. Now

$$\rho'(\mathbf{r}) = \rho_0 - \frac{1}{\sigma^2}\sum_{j=1}^{3} v^{(j)}\sum_{i=1}^{N} \exp\left(-\frac{1}{2\sigma^2}(\mathbf{R}'_i)^2\right)(\mathbf{R}'_i\cdot\hat{\mathbf{q}}_j)[\cos(\mathbf{q}_j\cdot\mathbf{R}'_i)\cos(\mathbf{q}_j\cdot\mathbf{r} + \varphi_j) \tag{S13}$$

$$+ \sin(\mathbf{q}_j\cdot\mathbf{R}'_i)\sin(\mathbf{q}_j\cdot\mathbf{r} + \varphi_j)]. \tag{S14}$$

The sum involving the term $(\mathbf{R}'_i\cdot\hat{\mathbf{q}}_j)\cos(\mathbf{q}_j\cdot\mathbf{R}'_i)$ is odd in $\mathbf{R}'_i$ and vanishes if the sum is taken over the entire infinitely-sized crystal. So Equation S14 becomes

$$\rho'(\mathbf{r}) = \rho_0 - \sum_{j=1}^{3}\left[\frac{v^{(j)}}{\sigma^2}\sum_{i=1}^{N} \exp\left(-\frac{1}{2\sigma^2}(\mathbf{R}'_i)^2\right)(\mathbf{R}'_i\cdot\hat{\mathbf{q}}_j)\sin(\mathbf{q}_j\cdot\mathbf{R}'_i)\right]\sin(\mathbf{q}_j\cdot\mathbf{r} + \varphi_j) \tag{S15}$$

$$= \rho_0 + \sum_{j=1}^{3}\tilde{\rho}_j\cos(\mathbf{q}_j\cdot\mathbf{r} + \varphi_j + \pi/2), \tag{S16}$$

where

$$\tilde{\rho}_j = \frac{v^{(j)}}{\sigma^2}\hat{\mathbf{q}}_j\cdot\sum_{i=1}^{N}\mathbf{R}'_i \exp\left(-\frac{1}{2\sigma^2}(\mathbf{R}'_i)^2\right)\sin(\mathbf{q}_j\cdot\mathbf{R}'_i). \tag{S17}$$

We note the sum in Equation S17 is simply a constant after the summation is performed. This constant depends on the high-symmetry structure and the smearing used.

Equation S16 shows that the smeared atomic density of the structure with a charge density wave is also a Fourier series generated by the three wavevectors. The phases of each component (ϕ_j) simply differ from those generating the charge density wave displacements (φ_j) by $\pi/2$. This is the relation between the phases shown in Tables S1 and S3 Importantly, Equation S17 shows that the amplitude of each component $\tilde{\rho}_j$ is directly proportional to the displacement amplitudes $v^{(j)}$. Therefore, the smeared atomic density associated with a structure with a charge density wave is indeed a Fourier series with the same wavevectors. The above derivation can be generalized to an inhomogeneous charge density wave where both $v^{(j)}$ and ϕ_j are functions of space. This is because the arguments or approximations in the derivation do not depend on the spatial dependence of these quantities.

CDW type	Hollow-center	Filled-center	Hexagonal
φ_1^0 $(2\pi/3)$	$-\frac{1}{3}$	$-\frac{1}{3}$	$-\frac{1}{3}$
φ_2^0 $(2\pi/3)$	$\frac{2}{3}$	$-\frac{1}{3}$	$-\frac{1}{3}$
φ_3^0 $(2\pi/3)$	$-\frac{1}{3}$	$\frac{5}{3}$	$-\frac{1}{3}$

TABLE S1: The reference values of the phases that generates the three types of normal state 3×3 charge density waves by Equation 2.

The total energies and relative energies between these three types of CDWs are shown below:

Type of CDW	Total energy (eV)	Relative energy from the most stable CDW (eV)
Hollow-center CDW	-6564.928	0
Filled-center CDW	-6564.906	0.022
Hexagonal CDW	-6564.898	0.030

TABLE S2: The total energies and relative energies of each type of CDW. For these calculations, 3×3 unit cells are included in the simulation cell. The most stable CDW is the hollow-center CDW in our calculations.

S2. EXTRACTING THE SMEARED ATOMIC DENSITY OF CHARGE DENSITY WAVES IN THE $MoSe_2$ LAYER

We have found that the charge density waves formed in the $MoSe_2$ layer to be very weak, that the background contribution to the oscillations in the smeared atomic density due to moiré relaxation becomes comparable to that due to the charge density waves. In order to remove this background, we run another relaxation with an electronic temperature of 5000 K. At this electronic temperature, charge density waves do not develop. We have checked that the moiré relaxation pattern is similar to that at 15.7 K. This high-temperature-relaxed structure gives the atomic displacement from the high-symmetry positions due to moiré relaxation only. These displacements are subtracted out from the low-temperature-relaxed structures, so that a structure with only charge density wave relaxations is obtained. The smeared atomic density is then calculated based on this structure.

S3. ESTIMATING THE PHASE FIELD WITH THE LOCAL PHASE APPROXIMATION

We prove Equation 5 for a uniform charge density wave, where the phases (ϕ_i), amplitudes (ρ_i) of the i-th components, and the mean (ρ_0) are constants. In this case, the Fourier series for the smeared atomic density in Equation 4 takes the form

$$\tilde{\rho}(\mathbf{r}) = \tilde{\rho}_0 + \sum_{i=1}^{3} \tilde{\rho}_i \cos(\mathbf{q}_i \cdot \mathbf{r} + \phi_i). \tag{S18}$$

By taking gradients of both sides, one obtains

$$\nabla\tilde{\rho}(\mathbf{r}) = -\sum_{i=1}^{3}\tilde{\rho}_i\mathbf{q}_i\sin(\mathbf{q}_i\cdot\mathbf{r}+\phi_i). \tag{S19}$$

If one projects both sides along the unit normal vector $\hat{\mathbf{n}}_1$ to the wavevector $\mathbf{q}_1$, for instance, then the $i=1$ component in Equation S19 vanishes since $\hat{\mathbf{n}}_1\cdot\mathbf{q}_1 = 0$. So Equation S19 becomes

$$\hat{\mathbf{n}}_1\cdot\nabla\tilde{\rho}(\mathbf{r}) = -\sum_{i=2}^{3}\tilde{\rho}_i(\hat{\mathbf{n}}_1\cdot\mathbf{q}_i)\cos(\mathbf{q}_i\cdot\mathbf{r}+\phi_i). \tag{S20}$$

Now if one takes the gradient on both sides again but projects both sides along the normal vector $\hat{\mathbf{n}}_2$ to the wavevector $\mathbf{q}_2$ instead, then the $i=2$ component also vanishes. This leaves one with the expression

$$\hat{\mathbf{n}}_2\cdot\nabla(\hat{\mathbf{n}}_1\cdot\nabla\tilde{\rho}(\mathbf{r})) = \tilde{\rho}_3(\hat{\mathbf{n}}_2\cdot\mathbf{q}_3)(\hat{\mathbf{n}}_1\cdot\mathbf{q}_3)\sin(\mathbf{q}_3\cdot\mathbf{r}+\phi_3). \tag{S21}$$

Equation S21 allows one to calculate ϕ_3 by taking the arcsin on both sides. Geometrically, it shows that the projected curvature along the directions $\mathbf{n}_1$ and $\mathbf{n}_2$ of a three-component Fourier series is determined by the oscillation along the remaining wavevector $\mathbf{q}_3$ only. This is what one would expect intuitively. If one picks a position $\mathbf{r}_0$, and consider gradient of $\tilde{\rho}$ along $\mathbf{n}_1$, then the contribution to the gradient due to the Fourier component of $\mathbf{q}_1$ is locally zero. This is because the gradient is being calculated along a plane of constant phase of the $\mathbf{q}_1$-component. If one subsequently considers the variation of this gradient along the direction $\mathbf{n}_2$, the variation of the gradient generated by the Fourier components of $\mathbf{q}_{1,2}$, i.e. the projected curvature, are both locally zero. This is because the projected curvature is being calculated along the planes of constant phases of the Fourier components of $\mathbf{q}_{1,2}$. The only contribution to the projected curvature is therefore associated with the Fourier component of $\mathbf{q}_3$ only.

Solving Equation S21 at any chosen position $\mathbf{r}_0$ gives two values of ϕ_3. In order to determine ϕ_3 unambiguously, one needs to know the value of $\cos(\mathbf{q}_3\cdot\mathbf{r}_0+\phi_3)$ as well. This is done by taking the gradient of Equation S21, which gives

$$\nabla(\hat{\mathbf{n}}_2\cdot\nabla(\hat{\mathbf{n}}_1\cdot\nabla\tilde{\rho}(\mathbf{r}))) = -\tilde{\rho}_3\mathbf{q}_3(\hat{\mathbf{n}}_2\cdot\mathbf{q}_3)(\hat{\mathbf{n}}_1\cdot\mathbf{q}_3)\cos(\mathbf{q}_3\cdot\mathbf{r}+\phi_3). \tag{S22}$$

The value of $\cos(\mathbf{q}_3\cdot\mathbf{r}+\phi_3)$ can be solved from Equation S22 if it is a scalar equation. Therefore, we project both sides along the wavevector $\mathbf{q}_3$ to obtain

$$\mathbf{q}_3\cdot\nabla(\hat{\mathbf{n}}_2\cdot\nabla(\hat{\mathbf{n}}_1\cdot\nabla\tilde{\rho}(\mathbf{r}))) = -\tilde{\rho}_3|\mathbf{q}_3|^2(\hat{\mathbf{n}}_2\cdot\mathbf{q}_3)(\hat{\mathbf{n}}_1\cdot\mathbf{q}_3)\cos(\mathbf{q}_3\cdot\mathbf{r}+\phi_3). \tag{S23}$$

Now, if we divide Equation S21 by Equation S23, the factor $\tilde{\rho}_3$ cancels out, and one obtains Equation 5. Knowing the values of both $\cos(\mathbf{q}_3\cdot\mathbf{r}+\phi_3)$ and $\sin(\mathbf{q}_3\cdot\mathbf{r}+\phi_3)$, we unambiguously determine the value of $\mathbf{q}_3\cdot\mathbf{r}+\phi_3$ using the *numpy* function *numpy.arctan2*. We then subtract out $\mathbf{q}_3\cdot\mathbf{r}$ to obtain the value of ϕ_3. We note that the value of ϕ_3 therefore obviously depends on the choice of origin. The other phases ϕ_1 and ϕ_2 can be obtained similarly by changing the normal vectors of projection to $\mathbf{n}_2$ and $\mathbf{n}_3$, and $\mathbf{n}_3$ and $\mathbf{n}_1$ respectively.

The values of the phase of the density oscillation associated with each type of CDW are summarized in Table S3. We note that there are infinitely many valid choices of phases for a given type of charge density wave. Intuitively, for instance, if a filled-center charge density is shifted to a different Se atom, the values of the phases will obviously change but the type of charge density wave remains the same. From this consideration, it is possible to show that the charge density wave generated by the phase triple $\{\phi_1^0, \phi_2^0, \phi_3^0\}$ can also be generated by the family of phases,

$$\phi_1(\mathbf{r}_p) = \phi_1^0 + \frac{2\pi}{3}M \tag{S24}$$

$$\phi_2(\mathbf{r}_p) = \phi_2^0 + \frac{2\pi}{3}N \tag{S25}$$

$$\phi_3(\mathbf{r}_p) = \phi_3^0 - \frac{2\pi}{3}(M+N), \tag{S26}$$

where N, M are integers.

CDW type	Hollow-center	Filled-center	Hexagonal
ϕ_1^0 $(2\pi/3)$	$\frac{23}{12}$	$\frac{23}{12}$	$\frac{23}{12}$
ϕ_2^0 $(2\pi/3)$	$\frac{35}{12}$	$\frac{23}{12}$	$\frac{23}{12}$
ϕ_3^0 $(2\pi/3)$	$\frac{23}{12}$	$\frac{11}{12}$	$\frac{23}{12}$

TABLE S3: The reference values of the phases that generates the three types of normal state 3×3 charge density waves using Equation 3.

For approximating an inhomogeneous charge density wave with Equation 4, we assume that the phase is locally constant so that Equation S18 is valid at each estimation point. This is equivalent to ignoring the terms first-order or higher-order in the gradient of the phase, $\nabla\phi_i$.

We have found that the local phase approximation works even for cases where the phase is linear in space, i.e. $\phi_i(\mathbf{r}) = -\mathbf{q}_i \cdot \mathbf{r}$. This phase field describes a charge density wave where the i-th component vanishes. We found that the phase profile estimated using this method reproduces the linear phase profile. Furthermore, the amplitude of the vanishing i-th component is correctly calculated to be zero using the estimated phase profile. This shows that the local phase approximation is appropriate for our purpose of estimating the amplitude of the charge density waves.

S4. LIST OF DERIVATIVES OF THE SMEARED ATOMIC DENSITY

In order to analytically calculate the value of the phases, we rewrite Equations S21 and S22 by replacing the fitting density $\tilde{\rho}(\mathbf{r})$ with the exact smeared atomic density $\rho(\mathbf{r})$. This leads to the appearance of the derivatives of the Gaussians. Below, we list the expressions used for evaluating the phases analytically for reference. We note only the atomic positions and the smearing need to be known for computing all quantities.

The gradient of the exact smeared atomic density can be written as

$$\nabla\rho(\mathbf{r}) = \hat{\mathbf{i}}\partial_x\rho + \hat{\mathbf{j}}\partial_y\rho. \tag{S27}$$

The dot product between the k-th normal vector $\mathbf{n}_k$ and the gradient of the density relevant for Equation S20 can then be written as

$$\hat{\mathbf{n}}_k \cdot \nabla\rho(\mathbf{r}) = \hat{n}_{kx}\partial_x\rho + \hat{n}_{ky}\partial_y\rho. \tag{S28}$$

The projected curvature along the normal vectors $\mathbf{n}_{j,k}$ relevant for Equation S21 can be written as

$$\hat{\mathbf{n}}_j \cdot \nabla(\hat{\mathbf{n}}_k \cdot \nabla\rho(\mathbf{r})) = \hat{n}_{jx}\hat{n}_{kx}\partial^2_{xx}\rho + (\hat{n}_{jy}\hat{n}_{kx} + \hat{n}_{jx}\hat{n}_{ky})\partial^2_{xy}\rho + \hat{n}_{jy}\hat{n}_{ky}\partial^2_{yy}\rho. \tag{S29}$$

The gradient of the projected curvature relevant for Equation S22 can be written as

$$\begin{aligned}\nabla(\hat{\mathbf{n}}_j \cdot \nabla(\hat{\mathbf{n}}_k \cdot \nabla\rho(\mathbf{r}))) = \hat{\mathbf{i}}[&\hat{n}_{jx}\hat{n}_{kx}\partial^3_{xxx}\rho + \hat{n}_{jy}\hat{n}_{ky}\partial^3_{xyy}\rho + (\hat{n}_{jx}\hat{n}_{ky} + \hat{n}_{jy}\hat{n}_{kx})\partial^3_{xxy}\rho] \\ &+ \hat{\mathbf{j}}[\hat{n}_{jy}\hat{n}_{ky}\partial^3_{yyy}\rho + \hat{n}_{jx}\hat{n}_{kx}\partial^3_{xxy}\rho + (\hat{n}_{jx}\hat{n}_{ky} + \hat{n}_{jy}\hat{n}_{kx})\partial^3_{xyy}\rho].\end{aligned} \tag{S30}$$

Thus the dot product between the $\mathbf{q}_i$ and the gradient of the projected curvature, which is relevant for Equation S23, is

$$\begin{aligned}\mathbf{q}_i \cdot \nabla(\hat{\mathbf{n}}_j \cdot \nabla(\hat{\mathbf{n}}_k \cdot \nabla\rho(\mathbf{r}))) = q_{ix}[&\hat{n}_{jx}\hat{n}_{kx}\partial^3_{xxx}\rho + \hat{n}_{jy}\hat{n}_{ky}\partial^3_{xyy}\rho + (\hat{n}_{jx}\hat{n}_{ky} + \hat{n}_{jy}\hat{n}_{kx})\partial^3_{xxy}\rho] \\ &+ q_{iy}[\hat{n}_{jy}\hat{n}_{ky}\partial^3_{yyy}\rho + \hat{n}_{jx}\hat{n}_{kx}\partial^3_{xxy}\rho + (\hat{n}_{jx}\hat{n}_{ky} + \hat{n}_{jy}\hat{n}_{kx})\partial^3_{xyy}\rho].\end{aligned} \tag{S31}$$

Inspecting Equations S27 to S30, the list of derivatives needed for computation is

$$\partial_x\rho = -(2\pi\sigma^4)^{-1}\sum_{i=1}^{N}(x - X_i)\exp\left(-\frac{(\mathbf{r} - \mathbf{R}_i)^2}{2\sigma^2}\right), \tag{S32}$$

$$\partial_y\rho = -(2\pi\sigma^4)^{-1}\sum_{i=1}^{N}(y - Y_i)\exp\left(-\frac{(\mathbf{r} - \mathbf{R}_i)^2}{2\sigma^2}\right), \tag{S33}$$

$$\partial^2_{xx}\rho = -\sigma^{-2}\rho + (2\pi\sigma^6)^{-1}\sum_{i=1}^{N}(x-X_i)^2\exp\left(-\frac{(\mathbf{r}-\mathbf{R}_i)^2}{2\sigma^2}\right), \tag{S34}$$

$$\partial^2_{xy}\rho = (2\pi\sigma^6)^{-1}\sum_{i=1}^{N}(x-X_i)(y-Y_i)\exp\left(-\frac{(\mathbf{r}-\mathbf{R}_i)^2}{2\sigma^2}\right), \tag{S35}$$

$$\partial^2_{yy}\rho = -\sigma^{-2}\rho + (2\pi\sigma^6)^{-1}\sum_{i=1}^{N}(y-Y_i)^2\exp\left(-\frac{(\mathbf{r}-\mathbf{R}_i)^2}{2\sigma^2}\right), \tag{S36}$$

$$\partial^3_{xxx}\rho = -3\sigma^{-2}\partial_x\rho + (2\pi\sigma^8)^{-1}\sum_{i=1}^{N}(x-X_i)^3\exp\left(-\frac{(\mathbf{r}-\mathbf{R}_i)^2}{2\sigma^2}\right), \tag{S37}$$

$$\partial^3_{xxy}\rho = -\sigma^{-2}\partial_y\rho + (2\pi\sigma^8)^{-1}\sum_{i=1}^{N}(x-X_i)^2(y-Y_i)\exp\left(-\frac{(\mathbf{r}-\mathbf{R}_i)^2}{2\sigma^2}\right), \tag{S38}$$

$$\partial^3_{xyy}\rho = -\sigma^{-2}\partial_x\rho + (2\pi\sigma^8)^{-1}\sum_{i=1}^{N}(x-X_i)(y-Y_i)^2\exp\left(-\frac{(\mathbf{r}-\mathbf{R}_i)^2}{2\sigma^2}\right), \tag{S39}$$

$$\partial^3_{yyy}\rho = -3\sigma^{-2}\partial_y\rho + (2\pi\sigma^8)^{-1}\sum_{i=1}^{N}(y-Y_i)^3\exp\left(-\frac{(\mathbf{r}-\mathbf{R}_i)^2}{2\sigma^2}\right). \tag{S40}$$

S5. EULER-LAGRANGE EQUATIONS FOR LOCAL AMPLITUDE AND MEAN ESTIMATION

In order to obtain the local amplitudes of each component and the local mean density at a fitting $\mathbf{r}_p$, the Lagrangian defined in Equation 6 is used for numerical optimization. We use the gradient descent method to derive the equations for numerically obtaining $\tilde{\rho}_0(\mathbf{r}_p)$ and $\tilde{\rho}_i(\mathbf{r}_p)$, which are

$$\tilde{\rho}_0^{(n+1)}(\mathbf{r}_p) = \tilde{\rho}_0^{(n)}(\mathbf{r}_p) - \gamma\left(\frac{\partial\mathcal{L}}{\partial\tilde{\rho}_0}\right)^{(n)} \tag{S41}$$

$$\tilde{\rho}_i^{(n+1)}(\mathbf{r}_p) = \tilde{\rho}_i^{(n)}(\mathbf{r}_p) - \gamma\left(\frac{\partial\mathcal{L}}{\partial\tilde{\rho}_i}\right)^{(n)}, \tag{S42}$$

where γ is the step length, $\tilde{\rho}_0^{(n)}(\mathbf{r}_p)$ and $\tilde{\rho}_i^{(n)}(\mathbf{r}_p)$ are the n-th iterates for the estimated local mean $\tilde{\rho}_0(\mathbf{r}_p)$ and the local amplitudes $\tilde{\rho}_i(\mathbf{r}_p)$ respectively, and $\left(\frac{\partial\mathcal{L}}{\partial\tilde{\rho}_i}\right)^{(n)}$ are the derivatives of the Lagrangian computed using Equation 6 at the n-th iteration. The step length is taken to be 0.1 in our calculations. The fitting area A_p is taken to be a parallelogram centered at the fitting point $\mathbf{r}_p$ and spanned by the lattice vectors $3\mathbf{a}_1$ and $3\mathbf{a}_2$.

The local mean density $\tilde{\rho}_0(\mathbf{r}_p)$ can then be shown to be given by

$$\tilde{\rho}_0(\mathbf{r}_p) = \frac{1}{A_p}\int_{A_p}\rho(\mathbf{r})d^2\mathbf{r}, \tag{S43}$$

which is what one will expect intuitively. Therefore, no iteration is required for estimating the local mean density.

For propagating the iterates of the local amplitude of the i-th component $\tilde{\rho}_i(\mathbf{r}_p)$, the partial derivative of $\mathcal{L}^{(n)}$ against $\tilde{\rho}_i$ is computed using

$$\left(\frac{\partial\mathcal{L}}{\partial\tilde{\rho}_i}\right)^{(n)} = -2\int_{A_p}\Delta^{(n)}(\mathbf{r})\sin(\mathbf{q}_i\cdot\mathbf{r}+\phi_i(\mathbf{r}))d^2\mathbf{r}, \tag{S44}$$

where $\phi_i(\mathbf{r})$ is the phase field computing using Equation 5, and $\Delta^{(n)}(\mathbf{r})$ is the penalty function computed at the n-th iteration. The penalty function is defined as

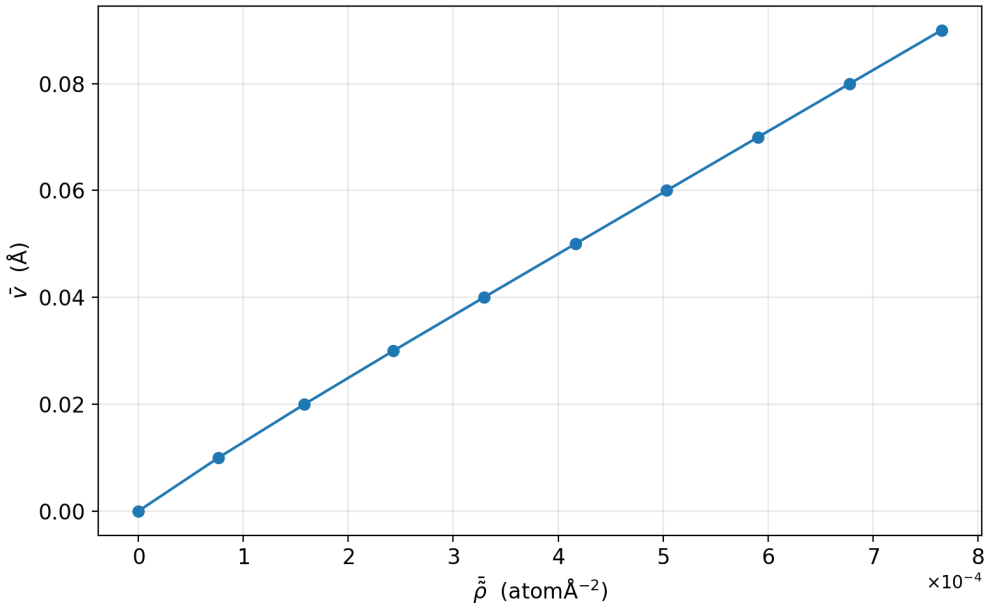
$$\Delta^{(n)}(\mathbf{r}) = \tilde{\rho}^{(n)}(\mathbf{r}) - \rho^{(n)}(\mathbf{r}). \tag{S45}$$

The convergence condition for $\tilde{\rho}_i$ is when the root-mean-square error $\varepsilon^{(n)}$, defined as,

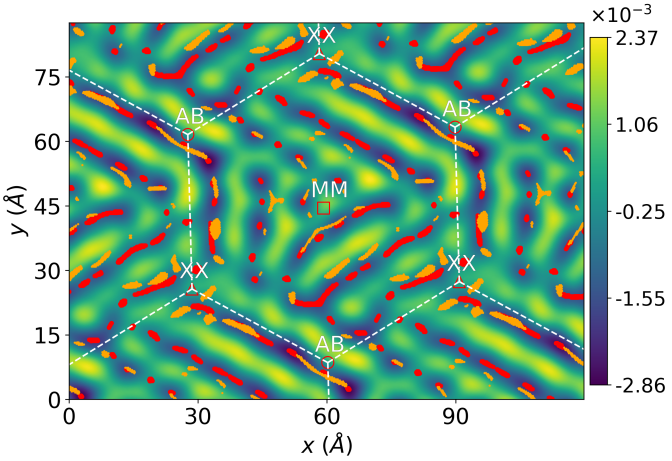
$$\varepsilon^{(n)} = \sqrt{\frac{1}{A_p}\int_{A_p}[\Delta^{(n)}(\mathbf{r})]^2 d^2\mathbf{r}}, \tag{S46}$$

is smaller than some threshold. The threshold is taken as 10^{-3} atomÅ^{-2} for the CDW of the Nb atoms, and 2×10^{-5} atomÅ^{-2} for that of the Mo atoms.

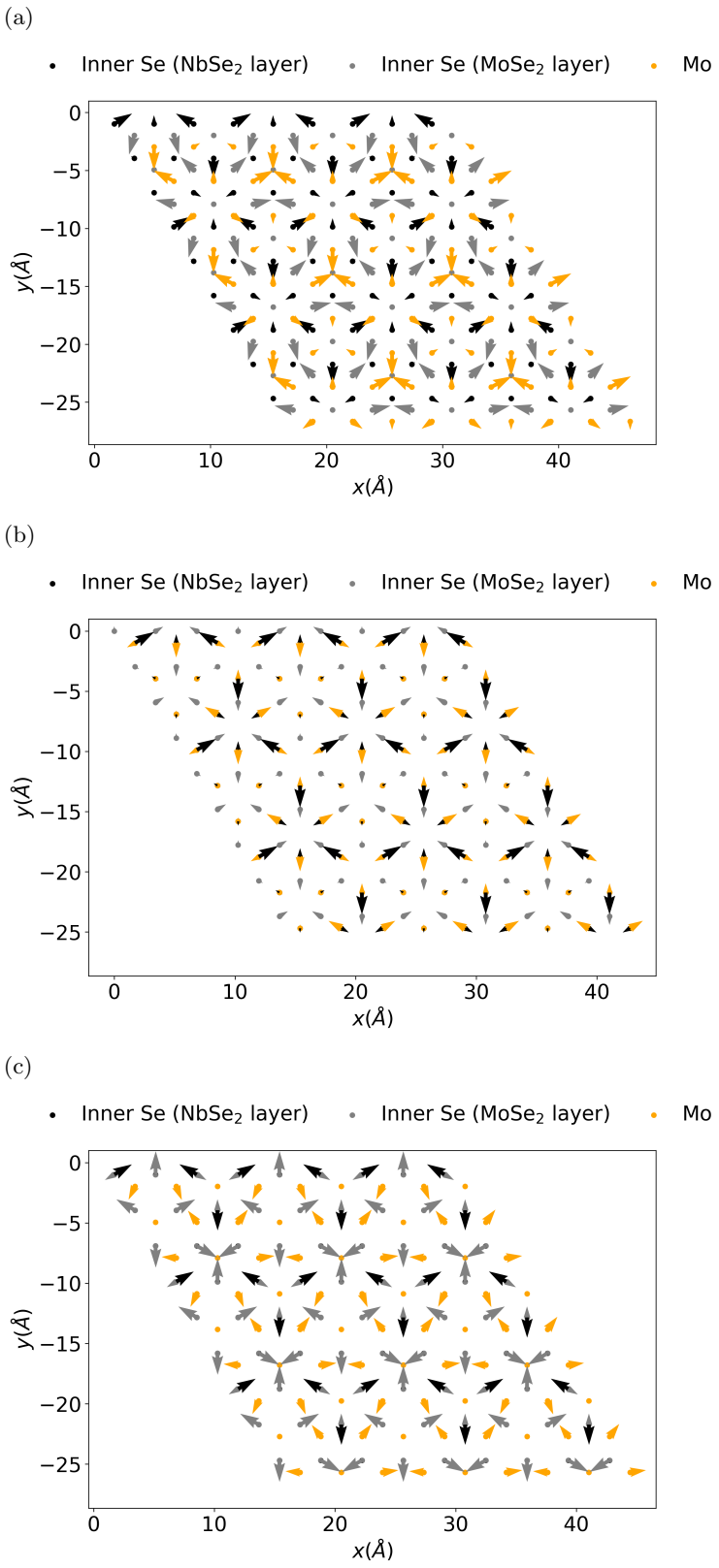
The displacement amplitude is related to the density oscillation amplitude by $v_j = 117$ Å^{3}atom$^{-1}\times\tilde{\rho}_j$ for $\sigma = 0.85a_0$. The constant of proportionality obtained by first generating a set of CDWs with different displacement amplitudes, followed by calculating the atomic density amplitude of these structures. The slope of the variation of the displacement amplitude against the atomic density amplitude (averaged over the three components) is then calculated. This variation is shown in Supplementary Figure S1.



SUPPLEMENTARY FIG. S1: The variation of the displacement amplitude, $\bar{v}$ against the amplitude of the atomic density $\bar{\tilde{\rho}}$.



SUPPLEMENTARY FIG. S2: Comparison of the positions of the extrema in the smeared Mo density to the smeared Nb density of the structure reported in the main text. The maxima (minima) in the smeared Mo density are marked in orange (red), and the smeared Nb density is plotted in the background. In these calculations, $\sigma = 0.85a_0$.



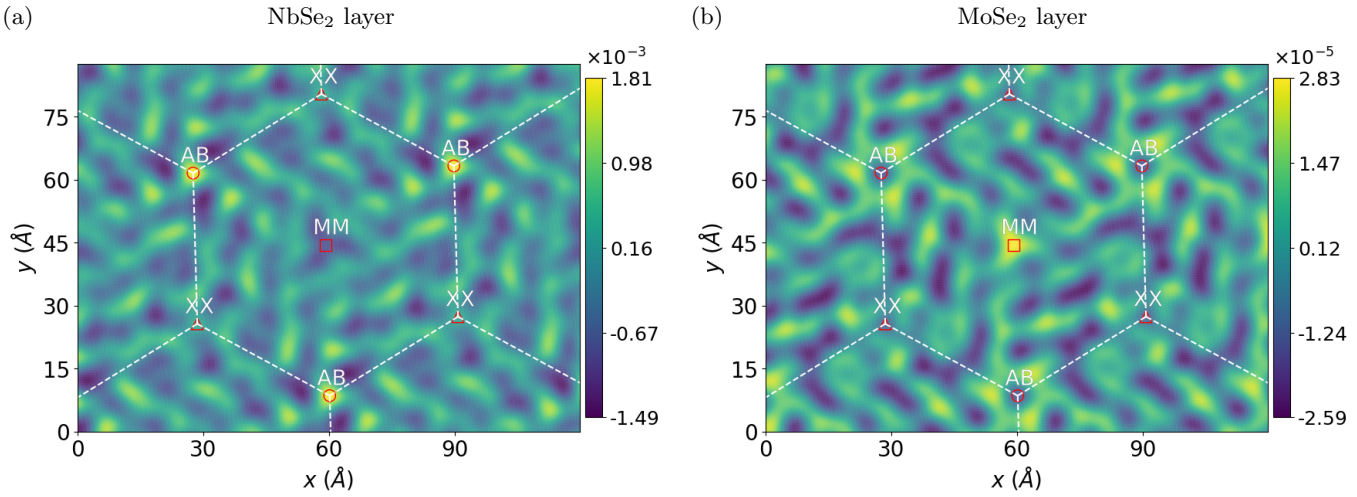
SUPPLEMENTARY FIG. S3: The atomic displacements of the inner Se atoms in the $NbSe_2$ layer (black), $MoSe_2$ layer (grey), and Mo atoms (orange) in the untwisted (a): MM-, (b): AB-, (c): XX-stacked bilayers of $NbSe_2/MoSe_2$.

S6. METASTABLE RELAXED TWISTED BILAYER STRUCTURE

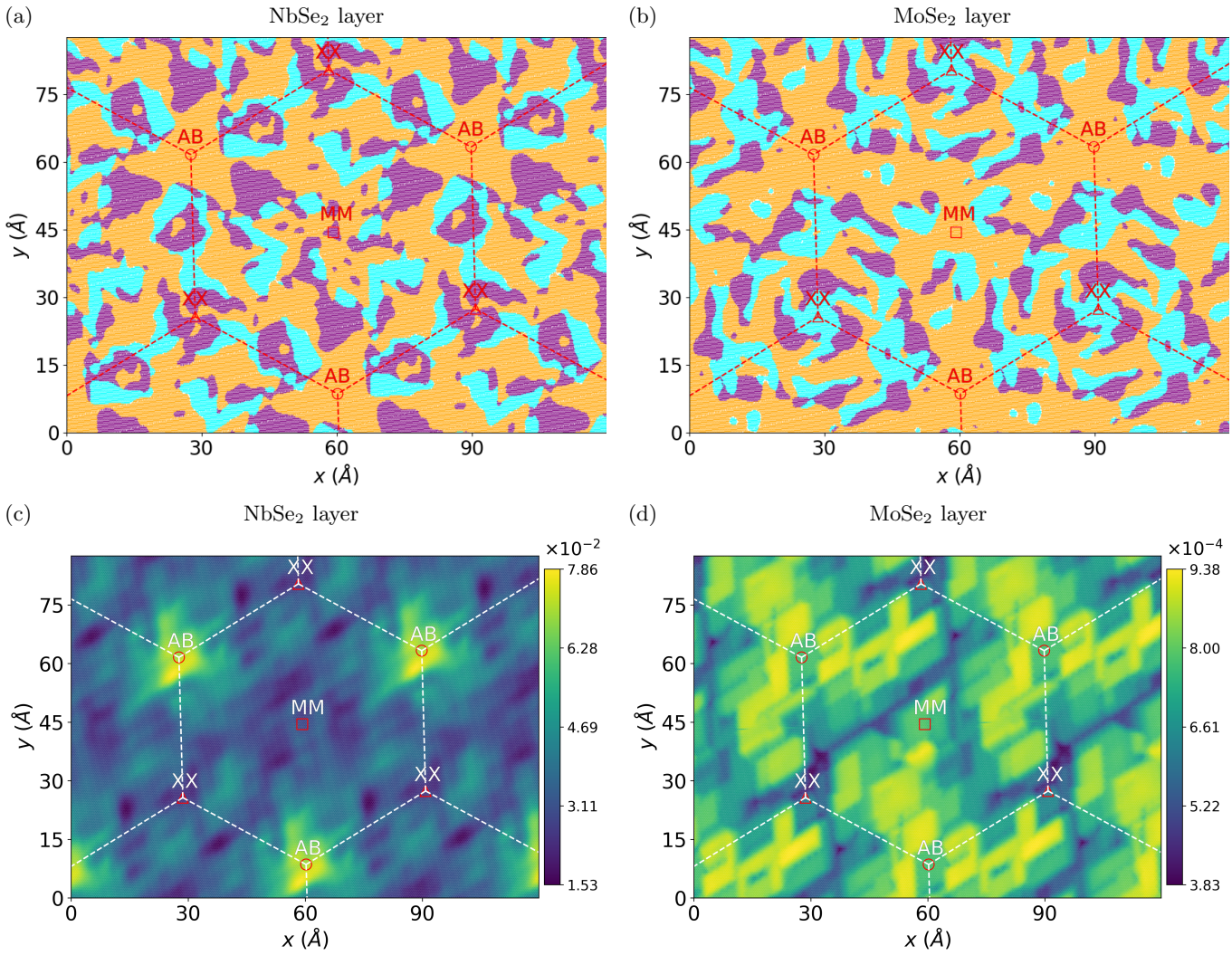
We note that more symmetrical metastable structures with somewhat different amplitude variations have been found. The total energy of the most stable structure reported in the main text is -1044573.2080 eV, while that of the metastable structure reported here is -1044573.0424 eV. The metastable structure is less stable by 0.2 eV, which is equivalent to 0.3 meV per unit cell.

Supplementary Figures S4(a) and (b) show the smeared atomic density of the Nb and Mo atoms in the metastable twisted bilayer $NbSe_2/MoSe_2$. This metastable structure has a different CDW domain distribution that demonstrates threefold rotation symmetry around all high-symmetry centers. See Supplementary Figures S5(a) and (b). However, the observation that the density minima in the smeared Nb density overlaps with the density maxima in the smeared Mo density still holds, see Supplementary Figure S6.

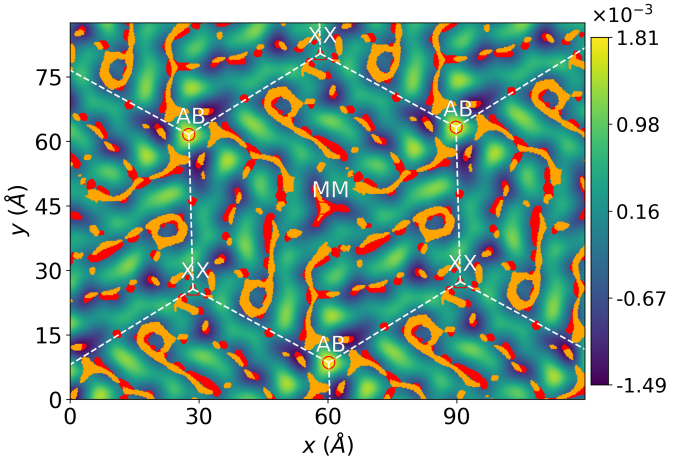
The CDW displacement amplitudes in the $NbSe_2$ and $MoSe_2$ layers are shown in Supplementary Figures S5(c) and (d). The local CDW displacement amplitudes in the $NbSe_2$ are 2.9×10^{-2} Å at the MM center; 5.9×10^{-2} Å at the AB center; 3.0×10^{-2} Å at the XX center. The local CDW displacement amplitudes in the $MoSe_2$ layer are 7.2×10^{-4} Å at the MM center; 8.4×10^{-4} Å at the AB center; and 5.9×10^{-4}Å at the XX center. In the $MoSe_2$ layer, the amplitudes and the AB and MM stacking regions have the same order of magnitude but are reduced compared to the most stable structure, and the amplitude becomes larger at the AB center than at the MM center, see Supplementary Figure S5. However, the displacement amplitude remains the smallest at the XX center. The predicted displacement amplitudes of the CDW in the $MoSe_2$ layer based on Figure 5 are 6.0×10^{-4} Å at the MM center; 8.4×10^{-4} Å at the AB center; and 4.0×10^{-4} Å at the XX center respectively. The values of the CDW displacement amplitudes in the $NbSe_2$ and $MoSe_2$ layers are therefore consistent with that predicted by Figure 5.



SUPPLEMENTARY FIG. S4: The (a): smeared Nb atom density, and (b): smeared Mo atom density computed using $\sigma = 0.85a_0$. The units are atomsÅ^{-2}.



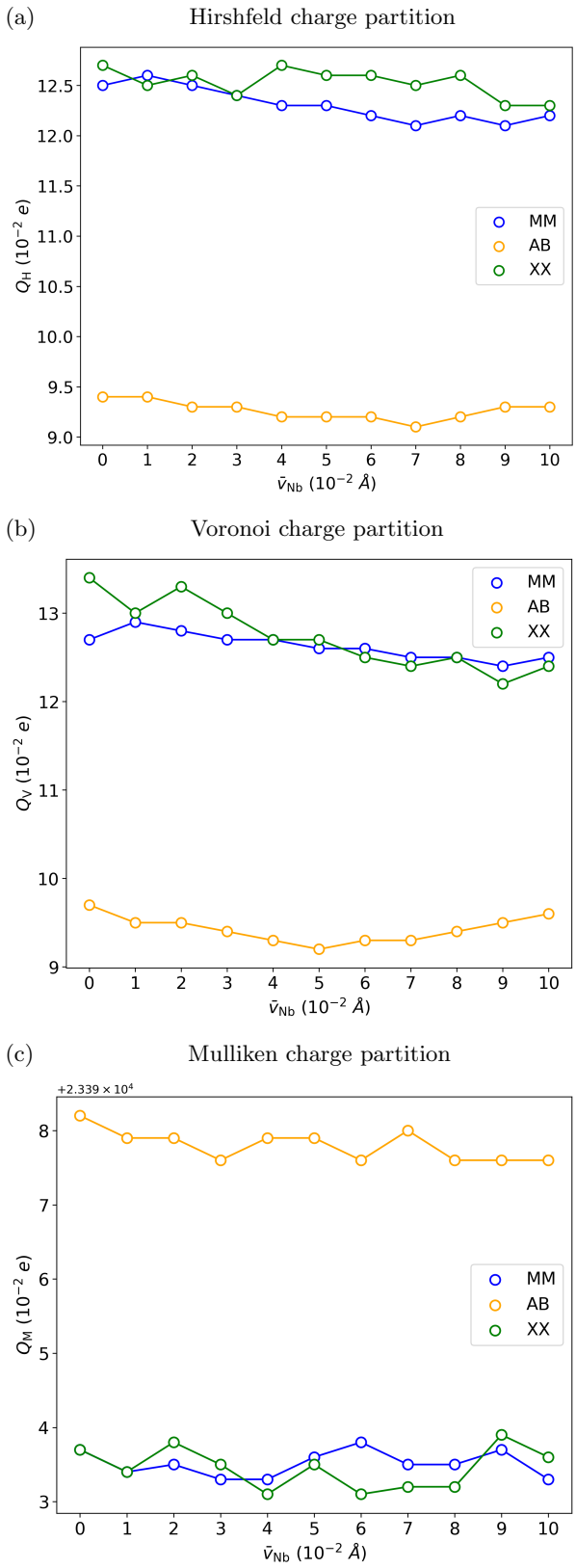
SUPPLEMENTARY FIG. S5: The type identification results in (a): the $NbSe_2$ layer and (b): in the $MoSe_2$ layer. The average CDW displacement amplitude of (c): Nb atoms and (d): Mo atoms in the metastable twisted $MoSe_2/NbSe_2$ bilayer. The units are Å.



SUPPLEMENTARY FIG. S6: Comparison of the positions of the extrema in the smeared Mo density to the smeared Nb density of the metastable structure. The maxima (minima) in the smeared Mo density are marked in orange (red), and the smeared Nb density is plotted in the background.

S7. CHARGE TRANSFER ESTIMATION IN UNTWISTED BILAYERS

We calculate the charge transfer between the $NbSe_2$ layer and the $MoSe_2$ layer using the Hirshfeld, Voronoi, and Mulliken partition schemes implemented in SIESTA. We sum over the atomic charges in the $NbSe_2$ layer or $MoSe_2$ layer respectively. The total charges on each layer are the same, as expected from charge neutrality of the system. We report the dependence of the total charge in the $MoSe_2$ layer against the displacement amplitude of the CDW in the $NbSe_2$ layer in Supplementary Figure S7.



SUPPLEMENTARY FIG. S7: The dependence of the total charge in the $MoSe_2$ layer calculated using (a): Hirshfeld, (b): Voronoi, and (c): Mulliken charge partition schemes against the CDW displacement amplitude in the $NbSe_2$ layer.

[1] Y. Cao, V. Fatemi, S. Fang, K. Watanabe, T. Taniguchi, E. Kaxiras, and P. Jarillo-Herrero, "Unconventional superconductivity in magic-angle graphene superlattices," Nature, vol. 556, pp. 43–50, Mar. 2018.

[2] Y. Cao, V. Fatemi, A. Demir, S. Fang, S. L. Tomarken, J. Y. Luo, J. D. Sanchez-Yamagishi, K. Watanabe, T. Taniguchi, E. Kaxiras, et al., "Correlated insulator behaviour at half-filling in magic-angle graphene superlattices," Nature, vol. 556, pp. 80–84, Mar. 2018.

[3] R. Bistritzer and A. H. MacDonald, "Moiré bands in twisted double-layer graphene," Proceedings of the National Academy of Sciences, vol. 108, pp. 12233–12237, July 2011.

[4] Z. A. H. Goodwin, L. Klebl, V. Vitale, X. Liang, V. Gogtay, X. van Gorp, D. M. Kennes, A. A. Mostofi, and J. Lischner, "Flat bands, electron interactions, and magnetic order in magic-angle mono-trilayer graphene," Physical Review Materials, vol. 5, p. 084008, Aug. 2021.

[5] Z. A. H. Goodwin, F. Corsetti, A. A. Mostofi, and J. Lischner, "Attractive electron-electron interactions from internal screening in magic-angle twisted bilayer graphene," Physical Review B, vol. 100, p. 235424, Dec. 2019.

[6] G. Trambly de Laissardière, D. Mayou, and L. Magaud, "Localization of dirac electrons in rotated graphene bilayers," Nano Letters, vol. 10, no. 3, pp. 804–808, 2010. PMID: 20121163.

[7] D. Chen, Z. Lian, X. Huang, Y. Su, M. Rashetnia, L. Ma, L. Yan, M. Blei, L. Xiang, T. Taniguchi, et al., "Excitonic insulator in a heterojunction moiré superlattice," Nature Physics, vol. 18, pp. 1171–1176, Aug. 2022.

[8] V. Villafañe, M. Kremser, R. Hübner, M. M. Petrić, N. P. Wilson, A. V. Stier, K. Müller, M. Florian, A. Steinhoff, and J. J. Finley, "Twist-dependent intra- and interlayer excitons in moiré $MoSe_2$ homobilayers," Physical Review Letters, vol. 130, p. 026901, Jan. 2023.

[9] P. Parzefall, J. Holler, M. Scheuck, A. Beer, K.-Q. Lin, B. Peng, B. Monserrat, P. Nagler, M. Kempf, T. Korn, et al., "Moiré phonons in twisted $MoSe_2$–WSe_2 heterobilayers and their correlation with interlayer excitons," 2D Materials, vol. 8, p. 035030, May 2021.

[10] J. Quan, L. Linhart, M.-L. Lin, D. Lee, J. Zhu, C.-Y. Wang, W.-T. Hsu, J. Choi, J. Embley, C. Young, et al., "Phonon renormalization in reconstructed MoS_2 moiré superlattices," Nature Materials, vol. 20, pp. 1100–1105, Mar. 2021.

[11] I. Maity, A. A. Mostofi, and J. Lischner, "Electrons surf phason waves in moiré bilayers," Nano Letters, vol. 23, no. 11, pp. 4870–4875, 2023. PMID: 37235740.

[12] I. Maity, A. A. Mostofi, and J. Lischner, "Chiral valley phonons and flat phonon bands in moiré materials," Physical Review B, vol. 105, p. L041408, Jan. 2022.

[13] Y. Xu, A. Ray, Y.-T. Shao, S. Jiang, K. Lee, D. Weber, J. E. Goldberger, K. Watanabe, T. Taniguchi, D. A. Muller, et al., "Coexisting ferromagnetic–antiferromagnetic state in twisted bilayer CrI_3," Nature Nanotechnology, vol. 17, no. 2, pp. 143–147, 2022.

[14] Q. Tong, F. Liu, J. Xiao, and W. Yao, "Skyrmions in the moiré of van der waals 2d magnets," Nano Letters, vol. 18, no. 11, pp. 7194–7199, 2018.

[15] M. Akram and O. Erten, "Skyrmions in twisted van der waals magnets," Physical Review B, vol. 103, no. 14, p. L140406, 2021.

[16] F. Xiao, K. Chen, and Q. Tong, "Magnetization textures in twisted bilayer CrX_3 (X = Br, I)," Physical Review Research, vol. 3, no. 1, p. 013027, 2021.

[17] Z. Li, X. Lu, D. F. Cordovilla Leon, Z. Lyu, H. Xie, J. Hou, Y. Lu, X. Guo, A. Kaczmarek, T. Taniguchi, K. Watanabe, L. Zhao, L. Yang, and P. B. Deotare, "Interlayer exciton transport in $MoSe_2/WSe_2$ heterostructures," ACS Nano, vol. 15, no. 1, pp. 1539–1547, 2021. PMID: 33417424.

[18] Z. Lian, Y. Meng, L. Ma, I. Maity, L. Yan, Q. Wu, X. Huang, D. Chen, X. Chen, X. Chen, et al., "Valley-polarized excitonic mott insulator in WS_2/WSe_2 moiré superlattice," Nature Physics, vol. 20, pp. 34–39, Nov. 2023.

[19] C.-S. Lian, C. Si, and W. Duan, "Unveiling charge-density wave, superconductivity, and their competitive nature in two-dimensional $NbSe_2$," Nano Letters, vol. 18, no. 5, pp. 2924–2929, 2018. PMID: 29652158.

[20] F. Cossu, A. G. Moghaddam, K. Kim, H. A. Tahini, I. Di Marco, H.-W. Yeom, and A. Akbari, "Unveiling hidden charge density waves in single-layer $NbSe_2$ by impurities," Physical Review B, vol. 98, p. 195419, Nov. 2018.

[21] W. L. McMillan, "Landau theory of charge-density waves in transition-metal dichalcogenides," Physical Review B, vol. 12, pp. 1187–1196, Aug. 1975.

[22] W. L. McMillan, "Theory of discommensurations and the commensurate-incommensurate charge-density-wave phase transition," Physical Review B, vol. 14, pp. 1496–1502, Aug. 1976.

[23] W. L. McMillan, "Microscopic model of charge-density waves in 2H-$TaSe_2$," Physical Review B, vol. 16, pp. 643–650, July 1977.

[24] B. Guster, C. Rubio-Verdú, R. Robles, J. Zaldívar, P. Dreher, M. Pruneda, J. A. Silva-Guillén, D.-J. Choi, J. I. Pascual, M. M. Ugeda, P. Ordejón, and E. Canadell, "Coexistence of elastic modulations in the charge density wave state of 2H-$NbSe_2$," Nano Letters, vol. 19, no. 5, pp. 3027–3032, 2019. PMID: 30998364.

[25] C. T. S. Cheung, Z. A. H. Goodwin, Y. Han, J. Lu, A. A. Mostofi, and J. Lischner, "Coexisting charge density waves in twisted bilayer $NbSe_2$," Nano Letters, vol. 24, no. 39, pp. 12088–12094, 2024. PMID: 39297477.

[26] P. Dreher, W. Wan, A. Chikina, M. Bianchi, H. Guo, R. Harsh, S. Mañas Valero, E. Coronado, A. J. Martínez-Galera, P. Hofmann, et al., "Proximity effects on the charge density wave order and superconductivity in single-layer $NbSe_2$," ACS Nano, vol. 15, no. 12, pp. 19430–19438, 2021.

[27] M. K. Bin Subhan, A. Suleman, G. Moore, P. Phu, M. Hoesch, H. Kurebayashi, C. A. Howard, and S. R. Schofield, "Charge density waves in electron-doped molybdenum disulfide," Nano Letters, vol. 21, no. 13, pp. 5516–5521, 2021. PMID: 34228455.

[28] R. Moriya, N. Yabuki, and T. Machida, "Superconducting proximity effect in a $NbSe_2$/graphene van der waals junction," Physical Review B, vol. 101, p. 054503, Feb. 2020.

[29] J. M. Campanera, G. Savini, I. Suarez-Martinez, and M. I. Heggie, "Density functional calculations on the intricacies of moiré patterns on graphite," Physical Review B, vol. 75, p. 235449, June 2007.

[30] J. M. Soler, E. Artacho, J. D. Gale, A. García, J. Junquera, P. Ordejón, and D. Sánchez-Portal, "The SIESTA method for ab initio order-N materials simulation," Journal of Physics: Condensed Matter, vol. 14, pp. 2745–2779, Mar. 2002.

[31] J. Klimeš, D. R. Bowler, and A. Michaelides, "Chemical accuracy for the van der waals density functional," Journal of Physics: Condensed Matter, vol. 22, p. 022201, Dec. 2009.

[32] A. E. Jacobs and M. B. Walker, "Phenomenological theory of charge-density-wave states in trigonal-prismatic, transition-metal dichalcogenides," Physical Review B, vol. 21, pp. 4132–4148, May 1980.

[33] We note that the smeared atomic density does not exhibit a three-fold rotation symmetric structure as was observed in our recent work in twisted bilayer $NbSe_2$ [25]. We were able to find a structure that exhibits a symmetric smeared atomic density but has a slightly higher total energy. We analyze this metastable structure in Section S6 of the Supplementary Materials, but note that all qualitative findings obtained for the non-symmetric low-energy structure are also found in the high-symmetry structure.

[34] N. Troullier and J. L. Martins, "Efficient pseudopotentials for plane-wave calculations," Physical Review B, vol. 43, pp. 1993–2006, Jan. 1991.